Surface Force Measurements Using Brownian Particles

Maxime Lavaud, Thomas Salez, Yann Louyer, Yacine Amarouchene

Surface Force Measurements Using Brownian Particles

Maxime Lavaud,[1] Thomas Salez,[1,2,*] Yann Louyer,[1] and Yacine Amarouchene[1,†]

[1] *Univ. Bordeaux, CNRS, LOMA, UMR 5798, F-33405 Talence, France.*
[2] *Global Station for Soft Matter, Global Institution for Collaborative Research and Education, Hokkaido University, Sapporo, Japan.*

(Dated: December 8, 2020)

Brownian motion in confinement and at interfaces is a canonical situation, encountered from fundamental biophysics to nanoscale engineering. Using the Lorenz-Mie framework, we optically record the thermally-induced tridimensional trajectories of individual microparticles, within water, and in the vicinity of a rigid wall. Based on this data, we implement a novel, robust and self-calibrated multifitting method, allowing for the thermal-noise-limited inference of spatially-resolved diffusion coefficients, equilibrium potentials, and forces – at the femtoNewton resolution.

Brownian motion is a central paradigm in modern science. It has implications in fundamental physics, biology, and even finance, to name a few. By understanding that the apparent erratic motion of colloids is a direct consequence of the thermal motion of surrounding fluid molecules, pioneers like Einstein and Perrin provided decisive evidence for the existence of atoms [1, 2]. Specifically, free Brownian motion in the bulk is characterized by a typical spatial extent evolving as the square root of time, as well as Gaussian displacements.

At a time of miniaturization and interfacial science, and moving beyond the idealized bulk picture, it is relevant to consider the added roles of boundaries to the above context. Indeed, Brownian motion at interfaces and in confinement is a widespread practical situation in microbiology and nanofluidics. In such a case, surface effects become dominant and alter drastically the Brownian statistics, with key implications towards: i) the understanding and smart control of the interfacial dynamics of microscale entities; and ii) high-resolution measurements of surface forces at equilibrium. Interestingly, a confined colloid will exhibit non-Gaussian statistics related to the presence of multiplicative noises [3–5]. Besides, the particle can be subjected to electrostatic or Van der Waals forces [6] exerted by the interface, and might experience slippage too [7, 8]. Considering the two-body problem, the nearby boundary can also induce some effective interaction [9]. Previous studies have designed novel methods to measure the diffusion coefficient of confined colloids [10–15], or to infer surface forces [16–18]. However, such a statistical inference is still an experimental challenge, and a method taking simultaneously into account the whole ensemble of relevant properties, over broad spatial and time ranges, is currently lacking.

In this Letter, we aim at filling the previously-identified gap by implementing a novel method of statistical inference on a set of optically-recorded trajectories of individual microparticles, within water, and near a rigid substrate. We primarily reconstruct the equilibrium probability distribution function of the position, as well as the time-resolved probability distribution functions of the displacements in directions transverse and normal to the wall, including in particular the mean-squared displacements. Special attention is dedicated to the non-Gaussian statistics, for time scales ranging from tens of milliseconds to several tens of minutes. Furthermore, we implement the advanced inference method recently proposed by Frishman and Ronceray [19]. Besides, optimization schemes are used to determine precisely the free physical parameters and the actual distance to the wall. All together, this procedure leads to the robust inference of the two central quantities of the problem: i) the space-dependent short-term diffusion coefficients, with a nanoscale spatial resolution; and ii) the total force experienced by the particle, at the thermal-noise limit. These main results are summarized in Fig. 1, the goal of the Letter being the detailed obtention of which.

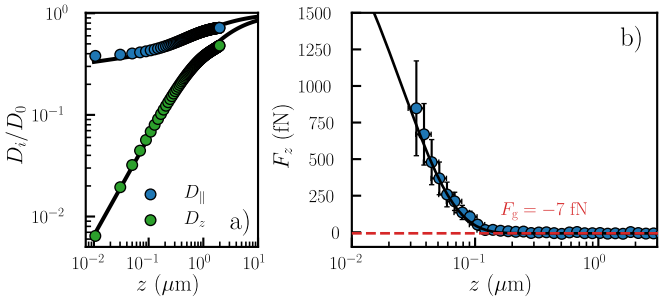

FIG. 1. a) Measured local short-term diffusion coefficients D_i of the microparticle, normalized by the bulk value D_0, as functions of the distance z to the wall (see Fig. 2c)), along both a transverse direction x or y ($D_i = D_\parallel = D_x = D_y$, blue) and the normal direction z ($D_i = D_z$, green) to the wall. The solid lines are the theoretical predictions, $D_\parallel(z) = D_0\eta/\eta_\parallel(z)$ and $D_z(z) = D_0\eta/\eta_z(z)$, using the local effective viscosities $\eta_\parallel(z)$ and $\eta_z(z)$ of Eqs. (3) and (4), respectively. b) Total normal conservative force F_z exerted on the particle as a function of the distance z to the wall, reconstructed from Eq. (11), using Eq. (4). The solid line corresponds to Eq. (12), with $B = 17$, $l_D = 26\,\text{nm}$ and $l_B = 550\,\text{nm}$. The dashed line indicates the buoyant weight $F_g = -7$ fN of the particle.

The experimental setup is schematized in Fig. 2a). A sample consists of a parallelepipedic chamber (1.5 cm × 1.5 cm × 150 μm), made from two glass covers, a parafilm

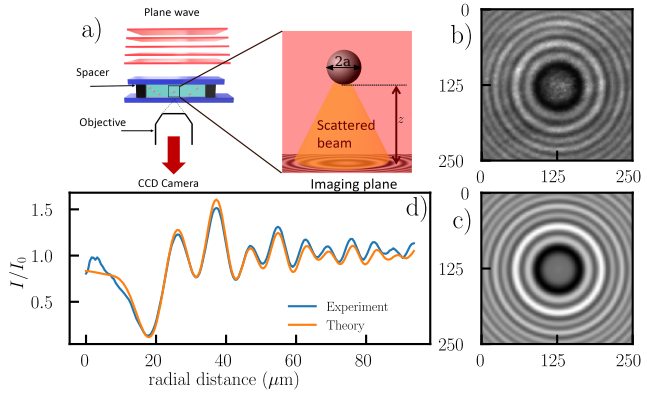

FIG. 2. a) Schematic of the experimental setup. A laser plane wave of intensity I_0 illuminates the chamber containing a dilute suspension of microspheres in water. The light scattered by a particle interferes with the incident beam onto the focal plane of an objective lens, that magnifies the interference pattern and relays it to a camera. b) Typical experimental interference pattern produced by one particle. c) Corresponding best-fit Lorenz-Mie interference pattern [20–23], providing a distance $z = 11.24 \pm 0.2$ μm to the wall, as well as the radius $a = 1.518 \pm 0.006$ μm and refractive index $n = 1.584 \pm 0.006$ of the particle. d) Angular averages of the intensities I (normalized by I_0) from the experimental and theoretical interference patterns, as functions of the radial distance to the z axis.

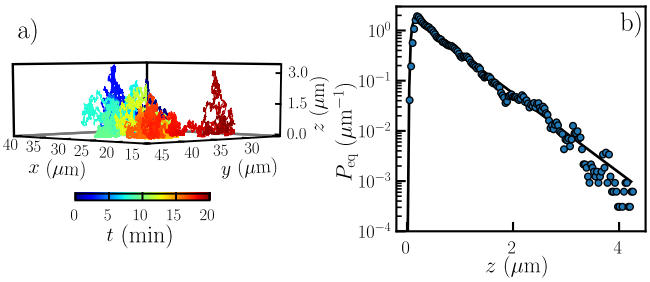

FIG. 3. a) Typical measured tridimensional trajectory $\mathbf{r}(t) = [x(t), y(t), z(t)]$ of the microparticle near the wall ($z = 0$). b) Measured equilibrium probability density function $P_{\rm eq}$ of the distance z between the particle and the wall. The solid line represents the best fit to the normalized Gibbs-Boltzmann distribution in position, using the total potential energy $U(z)$ of Eq. (1), with $B = 17$, $\ell_{\rm D} = 26$ nm, and $\ell_{\rm B} = 550$ nm.

spacer, and sealed with vacuum grease, containing a dilute suspension of spherical polystyrene beads (Sigma Aldrich) with nominal radii $a = 1.5 \pm 0.035$ μm, at room temperature T, in distilled water (type 1, MilliQ device) of viscosity $\eta = 1$ mPa.s. The sample is illuminated by a collimated laser beam with a 532 μm wavelength. The light scattered by one colloidal particle at a given time t interferes with the incident beam. An oil-immersion objective lens (x60 magnification, 1.30 numerical aperture) collects the resulting instantaneous interference pattern, and relays it to a camera with a 51.6 nm/pixel resolution (see Fig. 2b)). The exposure time for each frame is fixed to 3 ms to avoid motion-induced blurring of the image. The angular average of the intensity profile from each time frame is then fitted (see Figs. 2c,d)) to the Lorenz-Mie scattering function [20–23], which provides the particle radius a, its refractive index n, and its instantaneous tridimensional position $\mathbf{r} = (x, y, z)$. To reduce the uncertainty on the position measurement, we first calibrate $a = 1.518 \pm 0.006$ μm and $n = 1.584 \pm 0.006$ separately from the first 10^5 time frames. The obtained refractive index is consistent with the one reported in [15]. Then, for each subsequent time frame, the only remaining fitted quantity is $\mathbf{r}$, which allows us to reconstruct the trajectory $\mathbf{r}(t)$ with a nanometric spatial resolution, as shown in Fig. 3a).

Using the trajectory of the particle, one can then construct the equilibrium probability density function $P_{\rm eq}(\mathbf{r})$ of the position of the particle. We find that it does not depend on x and y, but only on the distance z between the particle and the wall. As seen in Fig. 3b), an exponential tail is observed at large distance, which is identified to the sedimentation contribution in Perrin's experiment [2], but here with the probability density function of a single particle instead of the concentration field. In contrast, near the wall, we observe an abrupt depletion, indicating a repulsive electrostatic contribution. Indeed, when immersed in water, both the glass substrate and the polystyrene bead are negatively charged. All together, the total potential energy $U(z)$ thus reads:

$$\frac{U(z)}{k_{\rm B}T} = \begin{cases} B\,{\rm e}^{-\frac{z}{\ell_{\rm D}}} + \dfrac{z}{\ell_{\rm B}}\,, & \text{for } z > 0 \\ +\infty\,, & \text{for } z \leq 0 \end{cases}\,, \qquad (1)$$

where $k_{\rm B}$ is the Boltzmann constant, B is a dimensionless number related to the surface electrostatic potentials of the particle and the wall [16], $\ell_{\rm D}$ is the Debye length, $\ell_{\rm B} = k_{\rm B}T/(g\Delta m)$ is the Boltzmann length, g is the gravitational acceleration, and Δm is the (positive) buoyant mass of the particle. From this total potential energy, one can then construct the Gibbs-Boltzmann distribution $P_{\rm eq}(z) = A \exp[-U(z)/(k_{\rm B}T)]$ in position, where A is a normalization constant, that fits the data very well, as shown in Fig. 3b).

We now turn to dynamical aspects, by considering the mean-squared displacement (MSD). For the three spatial directions, indexed by $i = x$, y, and z, corresponding to the coordinates $r_x = x$, $r_y = y$, and $r_z = z$, of the position $\mathbf{r}$, and for a given time increment Δt, the MSD is defined as:

$$\langle \Delta r_i(t)^2 \rangle_t = \langle [r_i(t + \Delta t) - r_i(t)]^2 \rangle_t\,, \qquad (2)$$

where the average $\langle\rangle_t$ is performed over time t. For a free Brownian motion in the bulk, and in the absence of other forces than the dissipative and random ones, the MSD is linear in time, *i.e.* $\langle \Delta r_i(t)^2 \rangle_t = 2D_0\Delta t$, where

$D_0 = k_B T/(6\pi\eta a)$ is the bulk diffusion coefficient given by the Stokes-Einstein relation [1], and η is the liquid viscosity. Further including sedimentation restricts the validity of the previous result along z to short times only, *i.e.* for $\Delta t \ll \ell_B^2/D_0$ such that the vertical diffusion is not yet affected by the gravitational drift.

The presence of a rigid wall at $z = 0$ adds a repulsive electrostatic force along z. It also decreases the mobilities nearby through hydrodynamic interactions, leading to effective viscosities $\eta_\parallel(z) = \eta_x(z) = \eta_y(z)$, and $\eta_z(z)$. The latter are [24]:

$$\eta_\parallel = \frac{\eta}{1 - \frac{9}{16}\xi + \frac{1}{8}\xi^3 - \frac{45}{256}\xi^4 - \frac{1}{16}\xi^5} \ , \tag{3}$$

where $\xi = a/(z+a)$, and:

$$\eta_z = \eta\,\frac{6z^2 + 9az + 2a^2}{6z^2 + 2az} \ , \tag{4}$$

which is Padé-approximated within 1% accuracy [25].

Interestingly, despite the previous modifications, the temporal linearity of the MSD is not altered by the presence of the wall [16, 26] for x and y, as well as at short times for z. In such cases, the MSD reads:

$$\langle \Delta r_i(t)^2 \rangle_t = 2\langle D_i \rangle \Delta t \ , \tag{5}$$

where for each spatial direction we introduced the local diffusion coefficient $D_i(z) = D_0\eta/\eta_i(z)$, and its average $\langle D_i(z)\rangle = \int_0^\infty \mathrm{d}z\, D_i(z) P_{\mathrm{eq}}(z)$ against the Gibbs-Boltzmann distribution in position. As shown in Fig. 4a), the MSD measured along x or y is indeed linear in time. By fitting to Eq. (5), using Eqs. (1) and (3), we extract an average transverse diffusion coefficient $\langle D_\parallel \rangle = \langle D_x \rangle = \langle D_y \rangle = 0.52\, D_0$. In contrast, along z, we identify two different regimes: one at short times, where the MSD is still linear in time, with a similarly-obtained best-fit value of $\langle D_z \rangle = 0.24\, D_0$; and one at long times, where the MSD saturates to a plateau. This latter behaviour indicates that the equilibrium regime has been reached, with the particle having essentially explored all the relevant positions given by the Gibbs-Boltzmann distribution.

Having focused on the MSD, *i.e.* on the second moment only, we now turn to the full probability density function P_i of the displacement Δr_i. Since, the diffusion coefficient $D_i(z)$ varies as a result of the variation of z along the particle trajectory, P_i exhibits a non-Gaussian behavior, as seen in Figs. 4b,c,d). We stress that we even resolve the onset of a non-Gaussian behaviour in P_x, by zooming on the large-$|\Delta x|$ wings (not shown). At short times, P_i can be modelled by the averaged diffusion Green's function [15, 27]:

$$P_i(\Delta r_i) = \int_0^\infty \mathrm{d}z\, P_{\mathrm{eq}}(z) \frac{1}{\sqrt{4\pi D_i(z)\Delta t}} \mathrm{e}^{-\frac{\Delta r_i^2}{4D_i(z)\Delta t}} \ , \tag{6}$$

against the Gibbs-Boltzmann distribution. As shown in Figs. 4b,c), Eq. (6) captures the early data very well. At

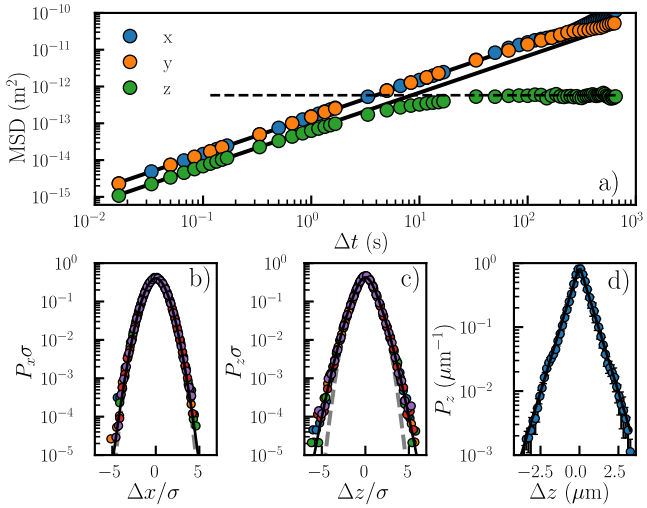

FIG. 4. a) Measured mean-squared displacements (MSD, see Eq. (2)) as functions of the time increment Δt, for the three spatial directions, x, y, and z. The solid lines are best fits to Eq. (5), using Eqs. (1), (3), and (4), with $B = 17$, $\ell_D = 26$ nm, and $\ell_B = 550$ nm, providing the average diffusion coefficients $\langle D_\parallel \rangle = \langle D_x \rangle = \langle D_y \rangle = 0.52\, D_0$ and $\langle D_z \rangle = 0.24\, D_0$. The dashed line is the best fit to Eq. (8), using Eq. (1), with $B = 17$, $\ell_D = 26$ nm, and $\ell_B = 550$ nm. b,c) Normalized probability density functions $P_i\,\sigma$ of the normalized displacements $\Delta x/\sigma$ and $\Delta z/\sigma$, at short times, with σ^2 the corresponding MSD (see panel a)), for different time increments Δt ranging from 0.0167 s to 0.083 s, as indicated with different colors. The solid lines are the best fits to Eq. (6), using Eqs. (1), (3), and (4), with $B = 17$, $\ell_D = 26$ nm, and $\ell_B = 550$ nm. For comparison, the grey dashed lines are normalized Gaussian distributions, with zero means and unit variances. d) Probability density function P_z of the displacement Δz, at long times, averaged over several values of Δt ranging between 25 and 30 s. The solid line is the best fit to Eq. (7), using Eq. (1), with $B = 17$, $\ell_D = 25.6$ nm, and $\ell_B = 550$ nm.

long times, Eq. (6) remains valid only for P_x and P_y. Nevertheless, the equilibrium regime being reached, P_z can eventually be written as:

$$\lim_{\Delta t\to\infty} P_z(\Delta z) = \int_0^\infty \mathrm{d}z\, P_{\mathrm{eq}}(z+\Delta z) P_{\mathrm{eq}}(z) \ , \tag{7}$$

which contains in particular the second moment:

$$\lim_{\Delta t\to\infty} \langle \Delta z^2 \rangle = \int_{-\infty}^{+\infty} \mathrm{d}\Delta z\, \Delta z^2 \int_0^\infty \mathrm{d}z\, P_{\mathrm{eq}}(z+\Delta z) P_{\mathrm{eq}}(z) \ . \tag{8}$$

As shown in Fig. 4d), Eq. (8) captures the long-term data along z very well.

We now wish to go beyond the previous average $\langle D_i \rangle$ of Eq. (5), and resolve the local diffusion coefficient $D_i(z)$. To measure local viscosities from experimental trajectories, a binning method is generally employed [28]. Although this technique is well suited for drift measurements, it suffers from a lack of convergence and precision

when second moments or local diffusion coefficients have to be extracted [19]. In particular, the binning method did not allow us to measure specifically the local diffusion coefficient in the key interfacial region corresponding to $z < 100$ nm. Besides, Frishman and Ronceray have recently developed a robust numerical method using stochastic force inference, in order to evaluate spatially-varying force fields and diffusion coefficients, from the information contained within the trajectories [19]. In practice, this is done by projecting the diffusion tensor onto a finite set of basis functions. We implemented this method, using fourth-order polynomials in our case. It allowed us to infer the local diffusion coefficients $D_i(z)$, down to $z = 10$ nm, as shown in Fig. 1a). The results are in excellent agreement with the theoretical predictions, $D_\parallel(z) = D_0\eta/\eta_\parallel(z)$ and $D_z(z) = D_0\eta/\eta_z(z)$, using the effective viscosities of Eqs. (3) and (4), thus validating the method.

So far, through Figs. 1a), 3b) and 4, we have successively presented the various measured statistical quantities of interest, as well as their fits to corresponding theoretical models. Therein, we have essentially three free physical parameters, B, ℓ_B, ℓ_D, describing the particle and its environment, as well as the *a priori* undetermined location of the $z = 0$ origin. These four parameters are actually redundant among the various theoretical models. Therefore, in order to measure them accurately, we in fact perform all the fits simultaneously, using a Broyden-Fletcher-Goldfarb-Shanno (BFGS) algorithm that is well suited for unconstrained nonlinear optimization [29]. To do so, we construct a global minimizer:

$$\chi^2 = \sum_{n=1}^{N} \chi_n^2 \ , \tag{9}$$

where we introduce the minimizer χ_n^2 of each set n among the N sets of data, defined as:

$$\chi_n^2 = \sum_{i=1}^{M_n} \frac{[y_{ni} - f_n(x_{ni}, \mathbf{b})]^2}{f_n(x_{ni}\ , \mathbf{b})^2} \ , \tag{10}$$

with $\{x_{ni}, y_{ni}\}$ the experimental data of set n, M_n the number of experimental data points for set n, f_n the model for set n, and $\mathbf{b} = (b_1, b_2, ..., b_p)$ the p free parameters. In our case, $p = 4$, and $\{x_{ni}, y_{ni}\}$ represent all the experimental data shown in Figs. 1a), 3b) and 4.

Due to strong dependence of the normal diffusion coefficient D_z with z, it is possible to find the wall position with a 10-nm resolution, thus overcoming a drawback of the Lorenz-Mie technique which only provides the axial distance relative to the focus of the objective lens. Besides, the three physical parameters globally extracted from the multifitting procedure are: $B = 17 \pm 1$, $\ell_\mathrm{D} = 26 \pm 1$ nm, and $\ell_\mathrm{B} = 550 \pm 1$ nm. Using the particle radius $a = 1.518 \pm 0.006$ μm calibrated from the preliminary fits of the interference patterns to the Lorenz-Mie scattering function (see Figs. 2c,d)), and the 1050 kg.m^{-3} tabulated bulk density of polystyrene, we would have expected $\ell_\mathrm{B} = 559$ nm instead, which corresponds to less than 2 % error, and might be attributed to nanometric offsets, such as *e.g.* the particle and/or wall rugosities.

Finally, we investigate the total conservative force $F_z(z)$ acting on the particle along z. Since there is no other non-conservative force than the Stokes drag acting on the particle, we can identify $F_z(z)$ to the latter, on average, and write:

$$F_z(z) = 6\pi\eta_z(z)a\frac{\langle\Delta z\rangle}{\Delta t} \ , \tag{11}$$

at fixed z. From the averaged measured vertical drifts $\langle\Delta z\rangle$, computed over a fine-enough z-binning grid, and invoking Eq. (4), one can reconstruct $F_z(z)$ from Eq. (11), as shown in Fig. 1b). In addition, the statistical error on the force measurement is comparable to $\sqrt{24\pi k_\mathrm{B}T\eta_z(z)a/\tau_\mathrm{box}(z)}$ [30], where $\tau_\mathrm{box}(z)$ is the total time spent by the particle in the corresponding box of the z-binning grid. To corroborate these measurements, we invoke Eq. (1) and express the total conservative force $F_z(z) = -U'(z)$ acting on the particle along z:

$$F_z(z) = k_\mathrm{B}T\left(\frac{B}{\ell_\mathrm{D}}\mathrm{e}^{-\frac{z}{\ell_\mathrm{D}}} - \frac{1}{\ell_\mathrm{B}}\right) \ . \tag{12}$$

Using the physical parameters extracted from the above multifitting procedure, we plot Eq. (12) in Fig. 1b). The agreement with the data is excellent, thus showing the robustness of the force measurement. In particular, we can measure forces down to a distance of 30 nm from the surface. Besides, far from the wall, we are able to resolve the actual buoyant weight $F_\mathrm{g} = -7 \pm 4$ fN of the particle. This demonstrates that we reach the femtoNewton resolution, and that this resolution is solely limited by thermal noise. As an ultimate remark, we are aware of an ongoing controversy regarding the claimed existence of additional statistical drifts [17, 31, 32], but we did not need to invoke such drifts here to rationalize our data.

To conclude, we have successfully built a multi-scale statistical analysis for the problem of freely diffusing individual colloids near a rigid wall. Combining the equilibrium distribution in position, time-dependent non-Gaussian statistics for the spatial displacements, a novel method to infer local diffusion coefficients, and a multifitting procedure, allowed us to reduce drastically the measurement uncertainties and reach the nanoscale and thermal-noise-limited femtoNewton spatial and force resolutions, respectively. The ability to measure tiny surface forces, locally, and at equilibrium, as well the possible extension of the method to non-conservative forces and out-of-equilibrium settings [33, 34], opens fascinating perspectives for nanophysics and biophysics.

We thank Elodie Millan, Louis Bellando de Castro, Julien Burgin, Bernard Trégon, Abdelhamid Maali,

David Dean and Mathias Perrin for interesting discussions. We acknowledge funding from the Bordeaux IdEx program - LAPHIA (ANR-10IDEX-03-02), Arts et Science (Sonotact 2017-2018) and Région Nouvelle Aquitaine (2018-1R50304).

* thomas.salez@u-bordeaux.fr
† yacine.amarouchene@u-bordeaux.fr

[1] A. Einstein. Über die von der molekularkinetischen Theorie der Wärme geforderte Bewegung von in ruhenden Flüssigkeiten suspendierten Teilchen. Annalen der Physik, vol. 4, t. 17, 1905.
[2] J. Perrin. Les Atomes. CNRS Editions, 2014. Google-Books-ID: A0ltBQAAQBAJ.
[3] B. U. Felderhof. Effect of the wall on the velocity autocorrelation function and long-time tail of brownian motion. The Journal of Physical Chemistry B, 109(45):21406–21412, 2005. PMID: 16853777.
[4] B. Wang, S. M. Anthony, S. C. Bae, and S. Granick. Anomalous yet Brownian. Proceedings of the National Academy of Sciences, 106(36):15160–15164, 2009.
[5] A. V. Chechkin, F. Seno, R. Metzler, and I. M. Sokolov. Brownian yet Non-Gaussian Diffusion: From Superstatistics to Subordination of Diffusing Diffusivities. Physical Review X, 7(2):021002, 2017.
[6] C. I. Bouzigues, P. Tabeling, and L. Bocquet. Nanofluidics in the debye layer at hydrophilic and hydrophobic surfaces. Phys. Rev. Lett., 101:114503, 2008.
[7] L. Joly, C. Ybert, and L. Bocquet. Probing the nanohydrodynamics at liquid-solid interfaces using thermal motion. Phys. Rev. Lett., 96:046101, 2006.
[8] J. Mo, A. Simha, and M. G. Raizen. Brownian motion as a new probe of wettability. The Journal of Chemical Physics, 146(13):134707, 2017.
[9] E. R. Dufresne, T. M. Squires, M. P. Brenner, and D. G. Grier. Hydrodynamic coupling of two brownian spheres to a planar surface. Phys. Rev. Lett., 85:3317–3320, 2000.
[10] L. P. Faucheux and A. J. Libchaber. Confined Brownian motion. Physical Review E, 49(6):5158–5163, 1994.
[11] E. R. Dufresne, D. Altman, and D. G. Grier. Brownian dynamics of a sphere between parallel walls. Europhysics Letters (EPL), 53(2):264–270, 2001.
[12] H. B. Eral, J. M. Oh, D. van den Ende, F. Mugele, and M. H. G. Duits. Anisotropic and hindered diffusion of colloidal particles in a closed cylinder. Langmuir, 26(22):16722–16729, 2010. PMID: 20936834.
[13] P. Sharma, S. Ghosh, and S. Bhattacharya. A high-precision study of hindered diffusion near a wall. Applied Physics Letters, 97(10):104101, 2010.
[14] J. Mo, A. Simha, and M. G. Raizen. Broadband boundary effects on brownian motion. Phys. Rev. E, 92:062106, 2015.
[15] M. Matse, M. V. Chubynsky, and J. Bechhoefer. Test of the diffusing-diffusivity mechanism using near-wall colloidal dynamics. Physical Review E, 96(4):042604, 2017.
[16] D. C. Prieve. Measurement of colloidal forces with TIRM. Advances in Colloid and Interface Science, 82(1):93–125, 1999.
[17] G. Volpe, L. Helden, T. Brettschneider, J. Wehr, and C. Bechinger. Influence of Noise on Force Measurements. Physical Review Letters, 104(17):170602, 2010.
[18] M. Li, O. Sentissi, S. Azzini, G. Schnoering, A. Canaguier-Durand, and C. Genet. Subfemtonewton force fields measured with ergodic Brownian ensembles. Physical Review A, 100(6):063816, 2019. Publisher: American Physical Society.
[19] A. Frishman and P. Ronceray. Learning Force Fields from Stochastic Trajectories. Physical Review X, 10(2):021009, 2020.
[20] C. F. Bohren and D. R. Huffman. Absorption and Scattering of Light by Small Particles. Wiley, 1998.
[21] M. Mishchenko. Scattering, absorption, and emission of light by small particles. Cambridge University Press, 2002.
[22] S.-H. Lee, Y. Roichman, G.-R. Yi, S.-H. Kim, S.-M. Yang, A. van Blaaderen, P. van Oostrum, and D. G. Grier. Characterizing and tracking single colloidal particles with video holographic microscopy. Optics Express, 15(26):18275, 2007.
[23] P. D. J. van Oostrum. Using light scattering to track, characterize and manipulate colloids (phd thesis), 2011.
[24] H. Brenner. The slow motion of a sphere through a viscous fluid towards a plane surface. Chemical Engineering Science, 16(3):242–251, 1961.
[25] M. A. Bevan and D. C. Prieve. Hindered diffusion of colloidal particles very near to a wall: Revisited. The Journal of Chemical Physics, 113(3):1228–1236, 2000.
[26] M. V. Chubynsky and G. W. Slater. Diffusing Diffusivity: A Model for Anomalous, yet Brownian, Diffusion. Physical Review Letters, 113(9):098302, 2014. Publisher: American Physical Society.
[27] S. Hapca, J. W. Crawford, and I. M. Young. Anomalous diffusion of heterogeneous populations characterized by normal diffusion at the individual level. Journal of The Royal Society Interface, 6(30):111–122, 2009. Publisher: Royal Society.
[28] R. Friedrich, J. Peinke, M. Sahimi, and M. Reza Rahimi Tabar. Approaching complexity by stochastic methods: From biological systems to turbulence. Physics Reports, 506(5):87–162, 2011.
[29] Y.-H. Dai. Convergence Properties of the BFGS Algoritm. SIAM Journal on Optimization, 13(3):693–701, 2002. Publisher: Society for Industrial and Applied Mathematics.
[30] L. Liu, S. Kheifets, V. Ginis, and F. Capasso. Subfemtonewton Force Spectroscopy at the Thermal Limit in Liquids. Physical Review Letters, 116(22):228001, 2016. Publisher: American Physical Society.
[31] R. Mannella and P. V. E. McClintock. Comment on "Influence of Noise on Force Measurements". Physical Review Letters, 107(7):078901, 2011.
[32] G. Volpe, L. Helden, T. Brettschneider, Jan Wehr, and C. Bechinger. Reply to Mannella and McClintock. Physical Review Letters, 107(7):078902, 2011.
[33] Y. Amarouchene, M. Mangeat, B.V. Montes, L. Ondic, T. Guérin, D.S. Dean, and Y. Louyer. Nonequilibrium dynamics induced by scattering forces for optically trapped nanoparticles in strongly inertial regimes. Physical Review Letters, 122(18), 2019.
[34] M. Mangeat, Y. Amarouchene, Y. Louyer, T. Guérin, and D.S. Dean. Role of nonconservative scattering forces and damping on brownian particles in optical traps. Physical Review E, 99(5), 2019.